High Spatiotemporal Resolution River Networks Mapping on Catchment Scale Using Satellite Remote Sensing Imagery and DEM Data

Peng Li[1, 2], Yun Zhang[1, 2], Cunren Liang[3], Houjie Wang[1, 2], and Zhenhong Li[4]

[1]Institute of Estuarine and Coastal Zone, College of Marine Geosciences, Key Lab of Submarine Geosciences and Prospecting Technology, Ministry of Education, Ocean University of China, Qingdao, China.

[2]Laboratory of Marine Geology, Qingdao National Laboratory for Marine Science and Technology, Qingdao, China.

[3]Institute of Remote Sensing and Geographic Information System, School of Earth and Space Sciences, Peking University, China.

[4]College of Geological Engineering and Geomatics, Chang'an University, Xi'an, China.

Corresponding author: Houjie Wang (hjwang@ouc.edu.cn)

Peng Li, and Yun Zhang are co-first authors of this article.

Key Points:

- A novel method is proposed to map the monthly river networks on the catchment scale using satellite imagery and DEM with 10 m resolution.
- This method provided detailed information on small- and medium-sized rivers with an overall accuracy of 95.8%.
- Correlation between monthly basin water area and precipitation was highly positive.

Abstract

Characterizing and understanding the changes in the flow regimes of rivers have been challenging. Existing global river network datasets are not updated and can only identify rivers wider than 30 m. We propose a novel automated method to map river networks on a monthly basin scale for the first time at 10-m resolution using Sentinel-1 Synthetic Aperture Radar, Sentinel-2 multispectral images, and the AW3D30 Digital Surface Model. This method achieved an overall accuracy of 95.8%. The total length of the Yellow River networks produced is 34,115 ±5800 km, approximately 3.2 times that of the Global River Widths from Landsat (GRWL) database, better covering small and medium rivers. The monthly river geometry revealed a positive correlation between basin area and precipitation. This study is expected to provide a cost-effective alternative to accurately mapping global river networks and advance our understanding of the changes and drivers of river systems.

Plain Language Summary

Understanding the impacts of climate change and human activities on water resources across different regions greatly depends on the knowledge of river networks with high spatial and temporal resolution. Small tributaries are important components in river network evolution and water transmission. To date, several studies have mapped interannual variations in rivers with widths >30 m; however, the distribution and variations in small rivers remain unclear. By integrating multispectral and radar satellite remote sensing images as well as topographic data, we created continuous monthly river network maps at the basin scale, allowing us to capture the details of dynamic changes in river networks with higher spatiotemporal resolution. As a result, the method used in this study provides detailed information on small and medium rivers, with the length of the connected rivers being thrice that of the existing datasets. We demonstrate the possibility of mapping global river networks monthly at a resolution of 10 m, providing valuable information for global surface water resource planning and management and improving our understanding of spatial links between land and water interfaces.

1 Introduction

River networks interact with the atmosphere, vegetation, and geomorphology; play important roles in global hydrological and biogeochemical cycles; and are natural hotspots for environmental sustainability and economic growth (Raymond et al., 2013; Allen et al., 2018). Spatial characteristics, such as river surface area and river channel morphology, are essential for discharge estimation, flood forecasting, riverbed evolution, hydrogeomorphic processes, and carbon emission assessment. From a long-term and global perspective, characterizing and understanding the dynamic changes in the flow regimes of rivers have been challenging (Wu et al., 2023). Therefore, there is a pressing need to understand what contributes to global river extent changes through better observation and modeling.

However, existing river network datasets, mainly from Landsat imagery, can only identify rivers with channel widths greater than 30 m (Pekel et al., 2016; Allen & Pavelsky, 2018), and ignore the temporal variations in rivers narrower than 30 m (Lu et al., 2020). Small river ecosystems are equally active, with frequent land-atmosphere interactions and 50% of the total carbon emissions (Raymond et al., 2013; Butman et al., 2016). Ignoring the importance of small rivers underestimates the role of river networks in biogeochemical cycles (Lu et al., 2021).

Thus, large-scale, accurate, and up-to-date river network maps are beneficial for sustainable development, government decision-making, and public awareness.

Currently available global and regional river network datasets are mainly derived from digital elevation models (DEMs) or remote sensing images (Li et al., 2022). The key to developing hydrological maps with DEM is to calculate the flow direction of each pixel (Strong & Mudd, 2022; Tarolli & Mudd, 2020), such as the HydroSHEDS and MERIT Hydro datasets. HydroSHEDS is a global hydrological dataset obtained from the SRTM elevation data with a resolution of 90 m (Lehner & Grill, 2013). Yamazaki et al. (2019) generated the MERIT Hydro dataset, which effectively solved the problem of limited coverage of HydroSHEDS at high latitudes. However, vertical uncertainties in the DEM data may distort the topographic slope and further affect the flow direction estimation. In addition, global DEM data sources are not updated in a timely manner, making it difficult to reflect the dynamic changes in river networks (Rinne et al. 2011; Schenk et al. 2014).

In recent years, Earth observation satellites have become an effective method for obtaining long-term time series, accurate distributions, and dynamic changes in global river networks (Gong et al., 2013; Yamazaki et al., 2015; Feng et al., 2019). Using Google Earth Engine (GEE) cloud-based computing resources, the storage, computing, and analysis capabilities of remote sensing big data have greatly improved (Gorelick et al., 2017). Pekel et al. (2016) produced a Global Surface Water (GSW) dataset at 30 m resolution using GEE and Landsat images, which presents the probability of surface water inundation for every pixel recorded by Landsat over the past four decades. Allen & Pavelsky (2018) built the Global River Widths from Landsat (GRWL) Database and estimated the total surface area of rivers and streams $\geqslant 30$ m wide at mean annual discharge, which is approximately 44% higher than previous estimates based on extrapolations of small sample sizes (Raymond et al., 2013). Compared with Landsat images, commercial optical remote sensing images usually have higher spatial resolution and richer spectral information; however, they are also affected by clouds and shadows when identifying water bodies.

Synthetic aperture radar (SAR) sensors operating in the microwave region of the electromagnetic spectrum are not limited by meteorological conditions and can penetrate clouds and vegetation cover. The fusion of SAR and optical images for water classification has been proven to capture surface water at a higher spatial and temporal resolution without being affected by clouds (Slinski et al., 2019a; Li et al., 2023). However, river networks extracted from remote-sensing images are fragmented and exhibit poor connectivity. Recent studies have suggested that a combination of satellite remote sensing imagery and DEM data can accurately extract continuous river networks and monitor their dynamic changes (Jones, 2019).

To address these challenges, we developed a new automated method that integrates Sentinel-1 SAR, Sentinel-2 multispectral images, and DEM data to generate monthly river network maps of the Yellow River basin (YRB) at a resolution of 10 m. The constraint of the topography on the river flow direction was used to solve the problem of poor connectivity. Furthermore, we evaluate the accuracy of the method and compare it with existing datasets. Finally, we investigated the correlation between river network areas and climatic factors.

2 Materials and Methods

2.1 Study Area

The Yellow River is the second largest river in China, originating in the Qinghai-Tibetan Plateau and flowing eastward through the Loess Plateau and North China Plain to the Bohai Sea (Wu et al., 2017; Syvitski et al., 2022). The main stream of the Yellow River has a total length of more than 5,400 km and a drainage area of more than 750,000 km^2 (Wang et al., 2007). The upper reaches of the Yellow River are dominated by mountains, whereas the middle and lower reaches are dominated by plains and hills (Figure 1a–c), forming the youngest delta in China (Wang et al., 2022). Nearly 90% of the sediment originates from the middle reaches, and 60% of the river runoff originates from the upper reaches (Wang et al., 2017; Zhu et al., 2021; Chang et al., 2022).

The Yellow River provides water to 15% of China's arable land and 12% of the population, accounting for 2.2% of the national runoff (Yin et al., 2021). It is characterized by water shortages, less water and more sediment, and different sources of water and sediment (Wang et al., 2019). With the gradual implementation of soil and water conservation and ecological restoration projects, the intensity of soil erosion in the Loess Plateau has decreased significantly, and the sediment load in the main stream of the Yellow River has shown a significant downward trend over the past 20 years (Syvitski et al., 2022). However, with the increasing frequency and intensity of extreme weather events, particularly rainstorms and droughts, changes in hydrological processes in the YRB are aggravating, posing challenges to water resource management, flood prevention, and water and sediment regulation in the basin (Lv et al., 2018; Shao et al., 2021).

2.2 Datasets

Sentinel-2 multispectral remote sensing images were used as the main data source (Drusch et al., 2012), and Sentinel-1 SAR images were used for detailed compensation. The Sentinel-2 Level-2A products provide orthorectified atmospherically corrected surface reflectance and can be freely obtained on the GEE platform. A total of 6,357 Sentinel-2 images were selected between January 2019 and December 2019. Considering the shortage of Sentinel-2 images with cloud cover of less than 20% in cloudy areas and data-missing regions, Sentinel-1 Ground Range Detected (GRD) products were selected as supplements.

The Advanced Land Observing Satellite (ALOS) World 3D-30 m (AW3D30) Digital Surface Model (DSM) was obtained by resampling the AW3D product with a spatial resolution of 30 m and a vertical accuracy of 5 m (Tadono et al., 2014). Among the publicly available global digital elevation model (DEM) datasets, AW3D30 has the highest accuracy in mountainous areas (Liu et al., 2019; P. Li et al., 2021). Therefore, we used AW3D30 as auxiliary data to represent the topographic relief and constrain the river flow direction in the YRB.

Other datasets included the GSW dataset, ERSI 2020 Land Cover data, and the fifth-generation ECMWF reanalysis (ERA5) dataset. The GSW dataset is used to verify the accuracy of the results. ESRI 2020 Land Cover data were used to generate scatter density maps of water and non-water samples and determine the threshold for water body extraction. These data can be accessed from the GEE's public data catalog. Temperature, precipitation, and evaporation were derived from ERA5 to evaluate the impact of climate change on river surface area.

2.3 Methods

Figure 2 shows the workflow of the proposed method. The process of river network generation mainly includes the following two parts: (1) water body extraction by median composite generation and threshold segmentation algorithms based on filtered Sentinel-2 multispectral and Sentinel-1 SAR images, and (2) river network extraction based on AW3D30 DSM flow modeling, noise removal, and connectivity processing.

2.3.1 Water Body Extraction

For the Sentinel-2 multispectral images, in order to effectively reduce the impact of omission errors from clouds and cloud shadow detection, opaque clouds and cirrus clouds were removed using the QA60 band on GEE. The position of the cloud shadow was determined based on the solar geometric angle and elevation angle attributes of each image, and dark pixels generated by the cloud shadow were masked. These filtered images were clipped to the study area to derive a median composite with a cloud cover limit of less than 20%.

The median image composite method was computationally efficient and robust. Sentinel-2 images processed by cloud filtering every month were collected, and the median of each pixel value was calculated to generate a composite image every month. This method was also applied to Sentinel-1 images after filtering. Compared to a single Sentinel-1 image, the median composite image can suppress speckle noise (Figure S1).

We used Simple Non-Iterative Clustering (SNIC) superpixels segmentation algorithm combining decision trees to segment water bodies (Wang et al., 2023) (Figure S2 and S6). Using superpixels as subsequent processing units can greatly accelerate data processing efficiency and reduce the complexity of identifying water bodies.

We then combined the automatic water extraction index (AWEI) (Feyisa et al., 2014), modified normalized difference water index (MNDWI) (Xu, 2006), normalized difference vegetation index (NDVI) (Rouse et al., 1974), and enhanced vegetation index (EVI) (Huete et al., 2002) to distinguish between water bodies and non-water areas in Sentinel-2 images (Zou et al., 2018; Deng et al., 2019). The AWEI is divided into AWEI_{nsh} and AWEI_{sh} based on the difference in noise sources produced by different types of areas. AWEI_{nsh} can effectively eliminate non-water pixels on dark building surfaces in urban background areas, that is for situations where shadows are not the main noise. AWEI_{sh} works mainly for situations in which shadows are the main problem. These indices are defined as follows:

$$AWEI_{nsh} = 4\times(\rho_{Green} - \rho_{SWIR1}) - (0.25\times\rho_{NIR} + 2.75\times\rho_{SWIR2}) \tag{1}$$

$$AWEI_{sh} = \rho_{Blue} + 2.5\times\rho_{Green} - 1.5\times(\rho_{NIR} + \rho_{SWIR1}) - 0.25\times\rho_{SWIR2} \tag{2}$$

$$MNDWI = \frac{\rho_{Green} - \rho_{SWIR1}}{\rho_{Green} + \rho_{SWIR1}} \tag{3}$$

$$EVI = 2.5\times\frac{(\rho_{NIR} - \rho_{Red})}{(1 + \rho_{NIR} + 6\times\rho_{Red} - 7.5\times\rho_{Blue})} \tag{4}$$

$$NDVI = \frac{\rho_{NIR} - \rho_{Red}}{\rho_{NIR} + \rho_{Red}} \tag{5}$$

where ρ_{Blue}, ρ_{Green}, ρ_{Red}, ρ_{NIR}, ρ_{SWIR1}, and ρ_{SWIR2} are the surface reflectance values of the Sentinel-2 Blue (band 2), green (band 3), red (band 4), NIR (band 8), SWIR1 (band 11), and SWIR2 (band 12) bands, respectively. These bands were resampled to 10 m.

We collected 19,998 samples, including 10,093 water samples and 9,905 non-water samples (see Text S1) and generated scatter density maps for water and non-water bodies (Figure S4). Of the non-water sample points, 99.81% had MNDWI-EVI<0, whereas 92.39% of the water sample points had MNDWI-EVI>0 (Figure S4e). Of the non-water sample points, 99.83% had MNDWI-NDVI<0, whereas 91.43% of the water sample points had MNDWI-NDVI>0 (Figure S4f). Furthermore, 95.31% of the water sample points show $AWEI_{nsh}$>-0.6 (Figure S4g), whereas 91.21% of the water sample points show $AWEI_{sh}$>0 (Figure S4h). Therefore, we proposed a new threshold segmentation algorithm for Sentinel-2 water body detection, that is, only the pixels meeting the criteria (($AWEI_{nsh}$>-0.6 or $AWEI_{sh}$>0) and (MNDWI>EVI or MNDWI>NDVI)) were classified as open surface water pixels, and the remaining were classified as non-water pixels. Paddy fields with spectral and water color characteristics similar to those of rivers can easily cause confusion and reduce the accuracy of river network extraction. The NDVI time-series features of the water objects were analyzed to eliminate paddy fields from the results (Figure S5).

We marked pixels in the missing areas of the Sentinel-2 images as no data and replaced them with SAR water extraction results after completing the Sentinel-2 water extraction. For Sentinel-1 SAR images, we used a refined Lee filter to suppress speckle noise while preserving the image details (Lee et al., 1999; Amitrano et al., 2018). This filter uses a non-square edge direction window to maintain the edge information, and all elements of the covariance matrix are filtered using the same parameters to prevent crosstalk between the channels. By calculating Sentinel-1 Dual-Polarized Water Index (SDWI) (Jia et al., 2019), the difference between water and non-water bodies are amplified, making the histogram of water bodies resemble a bimodal distribution. Then, the water threshold in block processing was obtained using the maximum inter-class difference threshold segmentation (OTSU) algorithm to segment and binarize the Sentinel-1 median composite images (Otsu, 1979).

2.3.2 River Networks Extraction

The river centerline was extracted using the RivWidthCloud algorithm proposed by Yang et al. (2020), which can be directly invoked on the GEE platform. The algorithm was based on the results of the binary river networks, which were divided into three steps: (1) calculation of the distance between each river pixel and the nearest non-river pixel, (2) convolution of the distance map to obtain the gradient map, and (3) skeletonization and refinement iterations (Figure S7).

Owing to the interference of non-water features, such as mountain shadows, snow, and ice, there are errors in the water body extraction results. We used the AW3D30 DSM data to fill in the depressions, calculate the D8 flow direction (Greenlee, 1987), estimate confluence accumulations, construct river network models, and generate buffers. This method can effectively reduce the errors caused by mountain shadows and maximally preserve the integrity of water information.

The flow model constructed using the AW3D30 DSM considers the adjacency relationship between river pixels and can generate continuous river networks. Therefore, we fused it with river network results extracted from remote sensing images, made directional connections to the fractured river networks, and generated an accurate and continuous river network with a spatial resolution of 10 m. Next, we compared the extracted results with those extracted from existing river network datasets and existing algorithms and quantitatively evaluated the accuracy of the results in terms of river length, river system density, and river network surface area.

3 Results

Figure S10 shows the dynamic changes in monthly river networks in the YRB in 2019. River density, that is, the ratio of river length to catchment area, increased from 0.038 km^{-1} in January and February to 0.042 km^{-1} in March and April, owing to upstream melting. The rivers developed rapidly in May and entered the wet season in July, which significantly improved the connectivity of river networks. At this time, the total length of the river was 40280 km and the density of the river system was 0.053 km^{-1}, both of which increased to the annual maximum. After September, the density of the river system gradually decreased and the river entered a normal period during the wet season.

To validate the reliability of our algorithm, we used 2,556 random “true water” sampling points and 2,430 random “true non-water” points (Text S2 and Figure S8). The results indicated that the overall accuracy was as high as 95.77%. The user accuracy, corresponding to the commission error, reached 95.83%, whereas the producer accuracy, representing the omission error, also reached a high level of 95.84% (Figure 4g and Table S1).

Furthermore, we compared our method (Figure 3c, 3g) with other algorithms for detecting river networks using Sentinel-2 imagery, including MNDWI (Figure 3d, 3h), an approach based on spectral indices and pixels (Zou et al., 2018) (Figure 3e, 3i), and the active-passive surface water classification (APWC) method proposed by Slinski et al. (2019) (Figure 3f and 3j). As there are many medium and large cities with dense populations in the main stream of the YRB, some pixels in the area are always covered by shadows because high-rise buildings are too high or the floor spacing is too small. The proposed algorithm effectively suppressed this type of shadow noise. Note that our algorithm does not require manual editing or data annotation, which makes it possible to realize the automatic mapping of large-scale river networks with high spatial resolution on a high-performance computing platform.

4 Discussion

The results were superimposed on the GRWL and GSW datasets to qualitatively evaluate the spatial distribution and details of the river networks (Figure 4). The results show that our method can more effectively enhance the contrast between the fine river and the surrounding background, and can extract more small rivers (Figure 4a-f). However, river networks were the most accurate and complete when the river width was greater than 30 m, whereas broken river lines may exist in areas less than 30 m wide. In addition, the influence of ice and snow cover on river extraction errors cannot be completely eliminated in the Qinghai-Tibet Plateau.

We further calculated the drainage density and open water fraction (OWF, i.e., the ratio of the water surface area to the catchment area) and quantified the accuracy of our extraction results using existing river network datasets. The drainage density of Yellow River networks map we determined is approximately three times higher than that of the existing GRWL and GSW datasets. The OWF index of the Yellow River network map was approximately 3.2 times that of the GRWL dataset. The GSW dataset contained artificial wetlands that were not considered part of the river networks in this study. Therefore, the OWF index of the GSW dataset is higher than that of our results. The superior performance of our method can be attributed to the following reasons: first, we used Sentinel-2 imagery with high spatial resolution to extract more small streams than Landsat images. Second, the use of Sentienl-1 to compensate for areas of Sentinel-2 images with clouds and missing data can improve temporal resolution and capture monthly changes in the YRB (Figure S9).

The rules established by Yan et al. (2019) were used to define and code river networks that could describe the topological relationships, hierarchical structures, and hydraulic connections of rivers at the same or different levels. The river lengths in our dataset were compared to those in the GRWL and Global River Network (GRN) datasets (Yan et al., 2019) in Figure 4h. Overall, the total length of the connected rivers provided in our results was 28,587 km longer than all rivers in the GRWL dataset, and 19,389 km longer than all rivers in the GRN dataset. Particularly, the length of connected river in our dataset is even longer than the length of level ⩾4 rivers in the GRWL dataset and GRN dataset, indicating that our results have a better coverage of medium and high-level rivers (Figure S11).

At the catchment scale, the scale dependence of runoff was attributed to spatial differences in precipitation, lithology, channel width, and catchment morphology. Assuming that the soil water content is negligible, the change in catchment area depends mainly on the difference between precipitation and evaporation. Figure 4i indicates that the change in the water surface area during the rainy season was significantly greater than that during the dry season. The minimum area of the river networks appeared in January, with a total area of 8,306 km^2 and the maximum area occurred in August, with a total area of 10,267 km^2. Precipitation and evaporation in the YRB were positively correlated with monthly changes in river network area. Considering that the average monthly precipitation is 10-20 times that of evaporation, the catchment area is primarily controlled by precipitation changes. The area of the river networks changed with seasonal fluctuations in precipitation, increasing after the spring and summer rainy seasons and decreasing in autumn and winter.

5 Conclusions

Studies on the impacts of climate change and human activity on river basins are highly dependent on the spatial and temporal distributions of river networks. However, the lack of accurate river networks with high spatiotemporal resolution in many regions makes these impacts poorly understood. In this study, we proposed a method for generating catchment-scale continuous river network maps for every month by integrating Sentinel-1 SAR and Sentinel-2 multispectral images with AW3D30 DSM data. This method can reveal detailed information on small and medium-sized rivers, with the length of the connected rivers being three times that of the existing datasets. The proposed detection rule can be used to extract large river network areas rapidly. The error caused by water spectral and morphological diversity as well as seasonal changes is reduced to the greatest extent, which makes large-scale and long-term water extraction more universal.

Compared to existing water extraction algorithms, the proposed method demonstrates its capability and effectiveness in the shadow noise environment of urban high-rise buildings and mountainous areas, indicating that it has certain advantages over other single water indices. In addition, compared to existing river network products, this method improves the extraction area of water and the extraction rate of small rivers. Therefore, it provides an alternative economic means for the long-term monitoring of river network changes, quantifying, and understanding the contribution of human activities and climate change to river channel evolution. In the future, further integration of the Surface Water and Ocean Topography mission will facilitate the rapid acquisition of river width, elevation, and discharge parameters on a global scale.

Open Research

The codes and river network maps of the Yellow River Basin are available in Zenodo (Li et al., 2023). Sentinel-1, Sentinel-2, AW3D30, and GSW datasets used in this study are available at GEE (https://developers.google.com/earth-engine/datasets/). ESRI 2020 Land Cover is freely available at https://livingatlas. arcgi. com. The ERA5 datasets are available from the Copernicus ECMWF Climate Data Store (Muñoz Sabater, 2019).

Acknowledgements

This study was supported by the Natural Science Foundation of China (No. 42041005-4). We thank Maoxiang Chang, Canran Tu, Quantao Zhu, Jie Liu, Shu Li, Hui'an Yang, Jianbo Bai, and Guoyang Wang from the Coastal Remote Sensing Group, Ocean University of China for their assistance with the field survey, data analysis, and manuscript review. The authors are very grateful to the anonymous reviewers, the editor (Valeriy Ivanov), and assistants (Meghan Ramil and Phillip Cobb) for their constructive and excellent reviews, which greatly improved the quality of the article.

References

Allen, G. H., & Pavelsky, T. M. (2018). Global extent of rivers and streams. *Science*, *361*(6402), 585–588. https://doi.org/10.1126/science.aat0636

Allen, G. H., Pavelsky, T. M., Barefoot, E. A., Lamb, M. P., Butman, D., Tashie, A., & Gleason, C. J. (2018). Similarity of stream width distributions across headwater systems. *Nature Communications*, *9*(1), 610. https://doi.org/10.1038/s41467-018-02991-w

Amitrano, D., Di Martino, G., Iodice, A., Riccio, D., & Ruello, G. (2018). Unsupervised Rapid Flood Mapping Using Sentinel-1 GRD SAR Images. *IEEE Transactions on Geoscience and Remote Sensing*, *56*(6), 3290–3299. https://doi.org/10.1109/TGRS.2018.2797536

Butman, D., Stackpoole, S., Stets, E., McDonald, C. P., Clow, D. W., & Striegl, R. G. (2016). Aquatic carbon cycling in the conterminous United States and implications for terrestrial carbon accounting. *Proceedings of the National Academy of Sciences*, *113*(1), 58–63. https://doi.org/10.1073/pnas.1512651112

Chang, M., Li, P., Sun, Y., Wang, H., & Li, Z. (2022). Mapping Dynamic Turbidity Maximum Zone of the Yellow River Estuary from 38 Years of Landsat Imagery. *Remote Sensing*, *14*(15), 3782. https://doi.org/10.3390/rs14153782

Deng, Y., Jiang, W., Tang, Z., Ling, Z., & Wu, Z. (2019). Long-Term Changes of Open-Surface Water Bodies in the Yangtze River Basin Based on the Google Earth Engine Cloud Platform. *Remote Sensing*, *11*(19), 2213. https://doi.org/10.3390/rs11192213

Drusch, M., Del Bello, U., Carlier, S., Colin, O., Fernandez, V., Gascon, F., et al. (2012). Sentinel-2: ESA's Optical High-Resolution Mission for GMES Operational Services. *Remote Sensing of Environment*, *120*, 25–36. https://doi.org/10.1016/j.rse.2011.11.026

Feng, S., Liu, S., Huang, Z., Jing, L., Zhao, M., Peng, X., et al. (2019). Inland water bodies in China: Features discovered in the long-term satellite data. *Proceedings of the National Academy of Sciences*, *116*(51), 25491–25496. https://doi.org/10.1073/pnas.1910872116

Feyisa, G. L., Meilby, H., Fensholt, R., & Proud, S. R. (2014). Automated Water Extraction Index: A new technique for surface water mapping using Landsat imagery. *Remote Sensing of Environment*, *140*, 23–35. https://doi.org/10.1016/j.rse.2013.08.029

Gong, P., Wang, J., Yu, L., Zhao, Y., Zhao, Y., Liang, L., et al. (2013). Finer resolution observation and monitoring of global land cover: first mapping results with Landsat TM and ETM+ data. *International Journal of Remote Sensing*, *34*(7), 2607–2654. https://doi.org/10.1080/01431161.2012.748992

Gorelick, N., Hancher, M., Dixon, M., Ilyushchenko, S., Thau, D., & Moore, R. (2017). Google Earth Engine: Planetary-scale geospatial analysis for everyone. *Remote Sensing of Environment*, *202*, 18–27. https://doi.org/10.1016/j.rse.2017.06.031

Greenlee, D. D. (1987). Raster and vector processing for scanned linework. *Photogrammetric Engineering and Remote Sensing*, *53*(10), 1383–1387.

Huete, A., Didan, K., Miura, T., Rodriguez, E. P., Gao, X., & Ferreira, L. G. (2002). Overview of the radiometric and biophysical performance of the MODIS vegetation indices. *Remote Sensing of Environment*, *83*(1), 195–213. https://doi.org/10.1016/S0034-4257(02)00096-2

Jia, S., Xue, D., Li, C., Zheng, J., & Li, W. (2019). Study on new method for water area information extraction based on Sentinel-1 data. *Yangtze River*, *50*(2), 213–217. https://doi.org/10.16232/j.cnki.1001-4179.2019.02.038.

Jones, J. W. (2019). Improved Automated Detection of Subpixel-Scale Inundation—Revised Dynamic Surface Water Extent (DSWE) Partial Surface Water Tests. *Remote Sensing*, *11*(4), 374. https://doi.org/10.3390/rs11040374

Lee, J.-S., Grunes, M. R., & de Grandi, G. (1999). Polarimetric SAR speckle filtering and its implication for classification. *IEEE Transactions on Geoscience and Remote Sensing*, *37*(5), 2363–2373. https://doi.org/10.1109/36.789635

Lehner, B., & Grill, G. (2013). Global river hydrography and network routing: baseline data and new approaches to study the world's large river systems. *Hydrological Processes*, *27*(15), 2171–2186. https://doi.org/10.1002/hyp.9740

Li, D., Xue, Y., Qin, C., Wu, B., Chen, B., & Wang, G. (2022). A bankfull geometry dataset for major exorheic rivers on the Qinghai-Tibet Plateau. *Scientific Data*, *9*(1). https://doi.org/10.1038/s41597-022-01614-w

Li, J., Li, L., Song, Y., Chen, J., Wang, Z., Bao, Y., et al. (2023). A robust large-scale surface water mapping framework with high spatiotemporal resolution based on the fusion of multi-source remote sensing data. *International Journal of Applied Earth Observation and Geoinformation*, *118*, 103288. https://doi.org/10.1016/j.jag.2023.103288

Li, P., Li, Z., Dai, K., Al-Husseinawi, Y., Feng, W., & Wang, H. (2021). Reconstruction and Evaluation of DEMs From Bistatic Tandem-X SAR in Mountainous and Coastal Areas of China. *IEEE Journal of Selected Topics in Applied Earth Observations and Remote Sensing*, *14*, 5152–5170. https://doi.org/10.1109/JSTARS.2021.3073782

Li, P., Zhang, Y., Liang, C., Wang, H., & Li, Z. (2023). High-Resolution Satellite-Derived River Network of the Yellow River Basin. [Software]. Zenodo. https://doi.org/10.5281/zenodo.10205284

Liu, K., Song, C., Ke, L., Jiang, L., Pan, Y., & Ma, R. (2019). Global open-access DEM performances in Earth's most rugged region High Mountain Asia: A multi-level assessment. *Geomorphology*, *338*, 16–26. https://doi.org/10.1016/j.geomorph.2019.04.012

Lu, X., Yang, K., Lu, Y., Gleason, C. J., Smith, L. C., & Li, M. (2020). Small Arctic rivers mapped from Sentinel-2 satellite imagery and ArcticDEM. *Journal of Hydrology*, *584*, 124689. https://doi.org/10.1016/j.jhydrol.2020.124689

Lu, X., Yang, K., Bennett, M. M., Liu, C., Mao, W., Li, Y., et al. (2021). High-resolution satellite-derived river network map reveals small Arctic river hydrography. *Environmental Research Letters*, *16*(5), 054015. https://doi.org/10.1088/1748-9326/abf463

Lv, M., Ma, Z., & Lv, M. (2018). Effects of Climate/Land Surface Changes on Streamflow With Consideration of Precipitation Intensity and Catchment Characteristics in the Yellow River Basin. *Journal of Geophysical Research: Atmospheres*, *123*(4), 1942–1958. https://doi.org/10.1002/2017JD027625

Muñoz Sabater, J. (2019): ERA5-Land hourly data from 1950 to present. [Dataset]. Copernicus Climate Change Service (C3S) Climate Data Store (CDS), https://doi.org/10.24381/cds.e2161bac

Otsu, N. (1979). A Threshold Selection Method from Gray-Level Histograms. *IEEE Transactions on Systems, Man, and Cybernetics*, *9*(1), 62–66. https://doi.org/10.1109/TSMC.1979.4310076

Pekel, J.-F., Cottam, A., Gorelick, N., & Belward, A. S. (2016). High-resolution mapping of global surface water and its long-term changes. *Nature*, *540*(7633), 418–422. https://doi.org/10.1038/nature20584

Raymond, P. A., Hartmann, J., Lauerwald, R., Sobek, S., McDonald, C., Hoover, M., et al. (2013). Global carbon dioxide emissions from inland waters. *Nature*, *503*(7476), 355–359. https://doi.org/10.1038/nature12760

Rouse, J. W., Haas, R. H., Schell, J. A., & Deering, D. W. (1974). Monitoring vegetation systems in the Great Plains with ERTS. *NASA Spec. Publ*, *351*(1), 309.

Shao, R., Zhang, B., He, X., Su, T., Li, Y., Biao, L., et al. (2021). Historical Water Storage Changes Over China's Loess Plateau. *Water Resources Research*, *57*. https://doi.org/10.1029/2020WR028661

Slinski, K. M., Hogue, T. S., & McCray, J. E. (2019). Active-Passive Surface Water Classification: A New Method for High-Resolution Monitoring of Surface Water Dynamics. *Geophysical Research Letters*, *46*(9), 4694–4704. https://doi.org/10.1029/2019gl082562

Strong, C. M., & Mudd, S. M. (2022). Explaining the climate sensitivity of junction geometry in global river networks. *Proceedings of the National Academy of Sciences*, *119*(50), e2211942119. https://doi.org/10.1073/pnas.2211942119

Syvitski, J., Restrepo, J., Saito, Y., Overeem, I., Vörösmarty, C., Wang, H., & Olago, D. (2022). Earth's sediment cycle during the Anthropocene. *Nature Reviews Earth & Environment*, *3*, 1–18. https://doi.org/10.1038/s43017-021-00253-w

Tadono, T., Ishida, H., Oda, F., Naito, S., Minakawa, K., & Iwamoto, H. (2014). Precise Global DEM Generation by ALOS PRISM. *ISPRS Annals of the Photogrammetry, Remote Sensing and Spatial Information Sciences*, *II–4*, 71–76. https://doi.org/10.5194/isprsannals-II-4-71-2014

Tarolli, P., & Mudd, S. M. (2020). *Remote Sensing of Geomorphology* (Vol. 23). Elsevier.

Wang, G., Li, P., Li, Z., Liang, C., & Wang, H. (2022). Coastal subsidence detection and characterization caused by brine mining over the Yellow River Delta using time series InSAR and PCA. *International Journal of Applied Earth Observation and Geoinformation*, *114*, 103077. https://doi.org/10.1016/j.jag.2022.103077

Wang, H., Yang, Z., Saito, Y., Liu, J. P., Sun, X., & Wang, Y. (2007). Stepwise decreases of the Huanghe (Yellow River) sediment load (1950–2005): Impacts of climate change and human activities. *Global and Planetary Change*, *57*(3), 331–354. https://doi.org/10.1016/j.gloplacha.2007.01.003

Wang, H., Wu, X., Bi, N., Li, S., Yuan, P., Wang, A., et al. (2017). Impacts of the dam-orientated water-sediment regulation scheme on the lower reaches and delta of the Yellow River (Huanghe): A review. *Global and Planetary Change*, *157*, 93–113. https://doi.org/10.1016/j.gloplacha.2017.08.005

Wang, M., Mao, D., Xiao, X., Song, K., Jia, M., Ren, C., & Wang, Z. (2023). Interannual changes of coastal aquaculture ponds in China at 10-m spatial resolution during 2016–2021. *Remote Sensing of Environment*, *284*, 113347. https://doi.org/10.1016/j.rse.2022.113347

Wang, Y., Zhao, W., Wang, S., Feng, X., & Liu, Y. (2019). Yellow River water rebalanced by human regulation. *Scientific Reports*, *9*(1), 9707. https://doi.org/10.1038/s41598-019-46063-5

Wu, Q., Ke, L., Wang, J., Pavelsky, T. M., Allen, G. H., Sheng, Y., et al. (2023). Satellites reveal hotspots of global river extent change. *Nature Communications*, *14*(1), 1587. https://doi.org/10.1038/s41467-023-37061-3

Wu, X., Bi, N., Xu, J., Nittrouer, J. A., Yang, Z., Saito, Y., & Wang, H. (2017). Stepwise morphological evolution of the active Yellow River (Huanghe) delta lobe (1976–2013): Dominant roles of riverine discharge and sediment grain size. *Geomorphology*, *292*, 115–127. https://doi.org/10.1016/j.geomorph.2017.04.042

Xu, H. (2006). Modification of normalised difference water index (NDWI) to enhance open water features in remotely sensed imagery. *International Journal of Remote Sensing*, *27*(14), 3025–3033. https://doi.org/10.1080/01431160600589179

Yamazaki, D., Trigg, M. A., & Ikeshima, D. (2015). Development of a global ~90m water body map using multi-temporal Landsat images. *Remote Sensing of Environment*, *171*, 337–351. https://doi.org/10.1016/j.rse.2015.10.014

Yamazaki, D., Ikeshima, D., Sosa, J., Bates, P. D., Allen, G. H., & Pavelsky, T. M. (2019). MERIT Hydro: A High-Resolution Global Hydrography Map Based on Latest Topography Dataset. *Water Resources Research*, *55*(6), 5053–5073. https://doi.org/10.1029/2019wr024873

Yan, D., Wang, K., Qin, T., Weng, B., Wang, H., Bi, W., et al. (2019). A data set of global river networks and corresponding water resources zones divisions. *Scientific Data*, *6*(1), 219. https://doi.org/10.1038/s41597-019-0243-y

Yang, X., Pavelsky, T. M., Allen, G. H., & Donchyts, G. (2020). RivWidthCloud: An Automated Google Earth Engine Algorithm for River Width Extraction From Remotely Sensed Imagery. *IEEE Geoscience and Remote Sensing Letters*, *17*(2), 217–221. https://doi.org/10.1109/LGRS.2019.2920225

Yin, S., Gao, G., Ran, L., Lu, X., & Fu, B. (2021). Spatiotemporal Variations of Sediment Discharge and In-Reach Sediment Budget in the Yellow River From the Headwater to the Delta. *Water Resources Research*, *57*(11), e2021WR030130. https://doi.org/10.1029/2021WR030130

Zhu, Q., Li, P., Li, Z., Pu, S., Wu, X., Bi, N., & Wang, H. (2021). Spatiotemporal Changes of Coastline over the Yellow River Delta in the Previous 40 Years with Optical and SAR Remote Sensing. *Remote Sensing*, *13*(10), 1940–1967. https://doi.org/10.3390/rs13101940

Zou, Z., Xiao, X., Dong, J., Qin, Y., Doughty, R. B., Menarguez, M. A., et al. (2018). Divergent trends of open-surface water body area in the contiguous United States from 1984 to 2016. *Proceedings of the National Academy of Sciences*, *115*(15), 3810–3815. https://doi.org/10.1073/pnas.1719275115

Figure 1. Location of the study area. (a) Upper reaches, (b) middle reaches, and (c) lower reaches in the Yellow River Basin were derived from Sentinel-2 RGB imagery. Note that, RGB bands include band 4 (red), band 3 (green), and band 2 (blue).

Figure 2. Workflow of river networks extraction in the Yellow River Basin.

Figure 3. Comparisons of the results of this method with other methods. Typical city (a) and mountain area (b) correspond to Figure 1a and 1b; (c) and (g) show the results of our method; (d) and (h) present the results of MNDWI; (e) and (i) are the results of Zou et al. (2018); (f) and (j) are the results of the APWC method proposed by Slinski et al. (2019).

Figure 4. Comparisons with different river datasets and our results. The base map shows Yellow River networks results and the existing the Global River Widths from Landsat (GRWL) database. (a), (c), and (e) Water surface results of the existing Global Surface Water (GSW) dataset. (b), (d), and (f) Water surface results of our method. (g) Confusion matrix for the automated accuracy assessment of our method. (h) Comparison of the river length (km) in the results of this study, GRWL dataset and Global River Networks (GRN) dataset. (i) The relationship between the surface area (yellow line), precipitation (blue column), temperature (red line), and evaporation (green line) in the Yellow River Basin.

Figure 1.

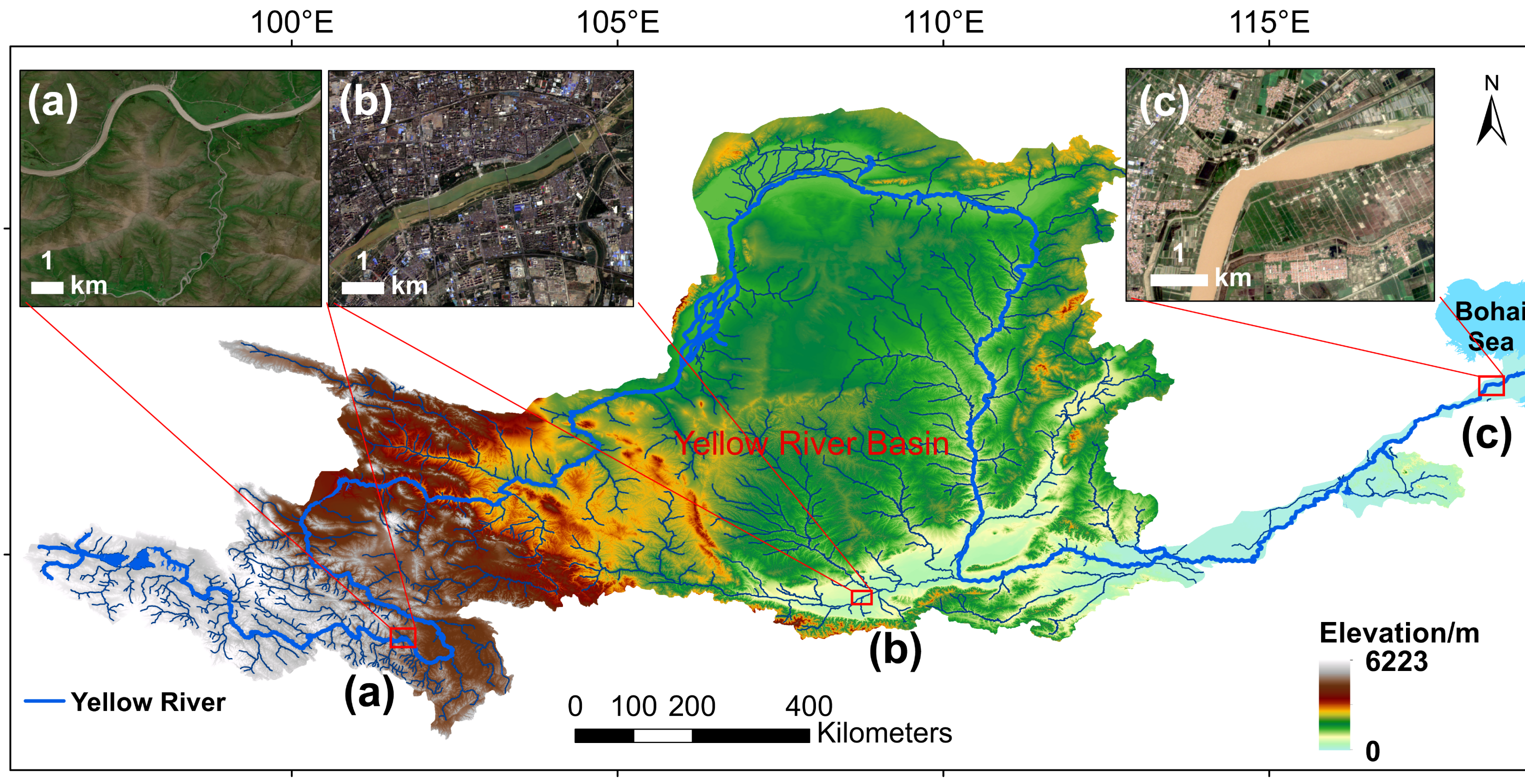
100°E
105°E
110°E
115°E
40°N
35°N
(a)
1 km
(b)
1 km
(c)
1 km
N
Bohai Sea
Yellow River Basin
(a)
(b)
(c)
Yellow River
0 100 200 400
Kilometers
Elevation/m
6223
0

Figure 2.

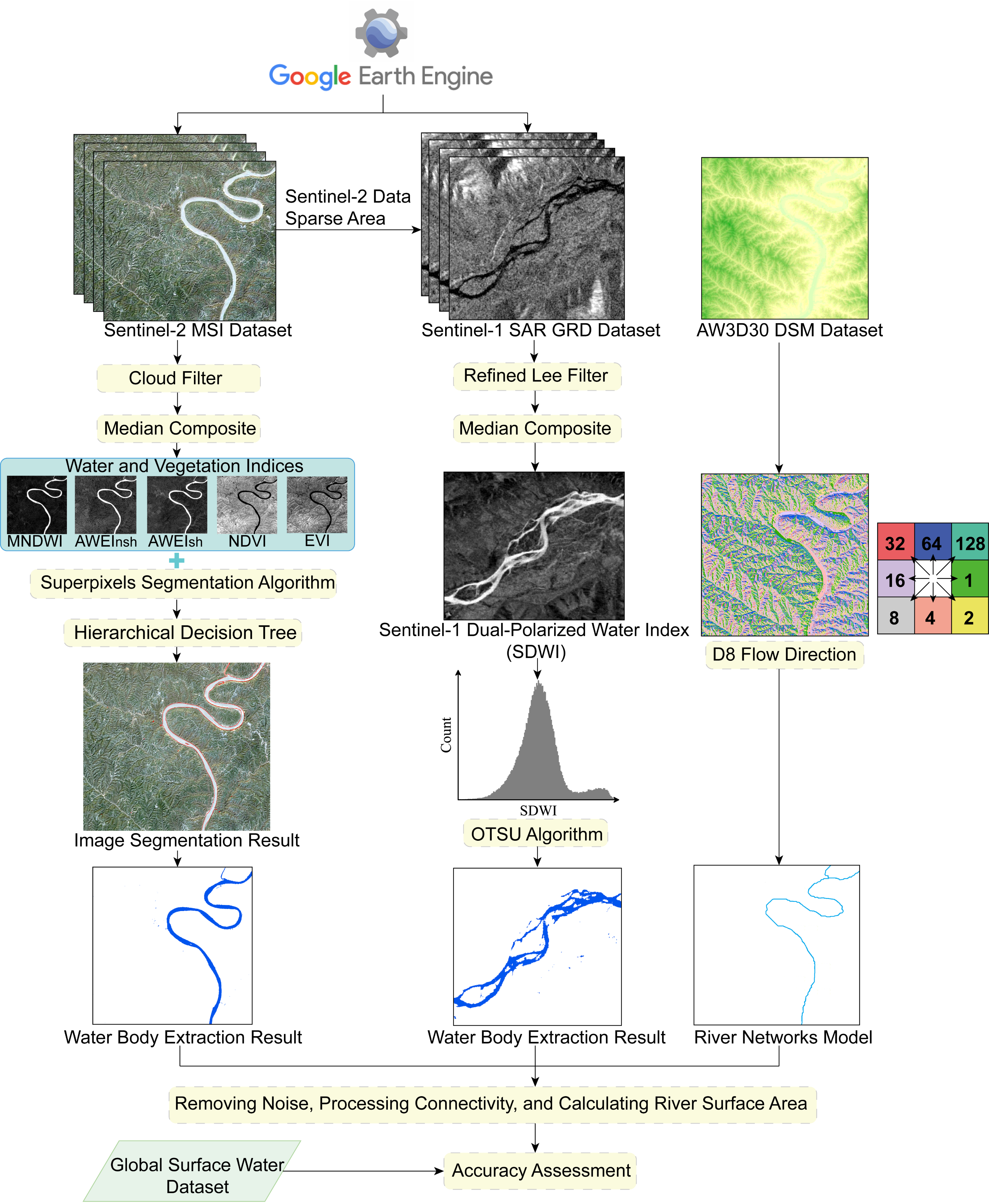

Google Earth Engine
Sentinel-2 Data Sparse Area
Sentinel-2 MSI Dataset
Sentinel-1 SAR GRD Dataset
AW3D30 DSM Dataset
Cloud Filter
Median Composite
Refined Lee Filter
Median Composite
Water and Vegetation Indices
MNDWI
AWEInsh
AWEIsh
NDVI
EVI
Superpixels Segmentation Algorithm
Hierarchical Decision Tree
Image Segmentation Result
Sentinel-1 Dual-Polarized Water Index (SDWI)
Count
SDWI
OTSU Algorithm
32
64
128
16
1
8
4
2
D8 Flow Direction
Water Body Extraction Result
Water Body Extraction Result
River Networks Model
Removing Noise, Processing Connectivity, and Calculating River Surface Area
Global Surface Water Dataset
Accuracy Assessment

Figure 3.

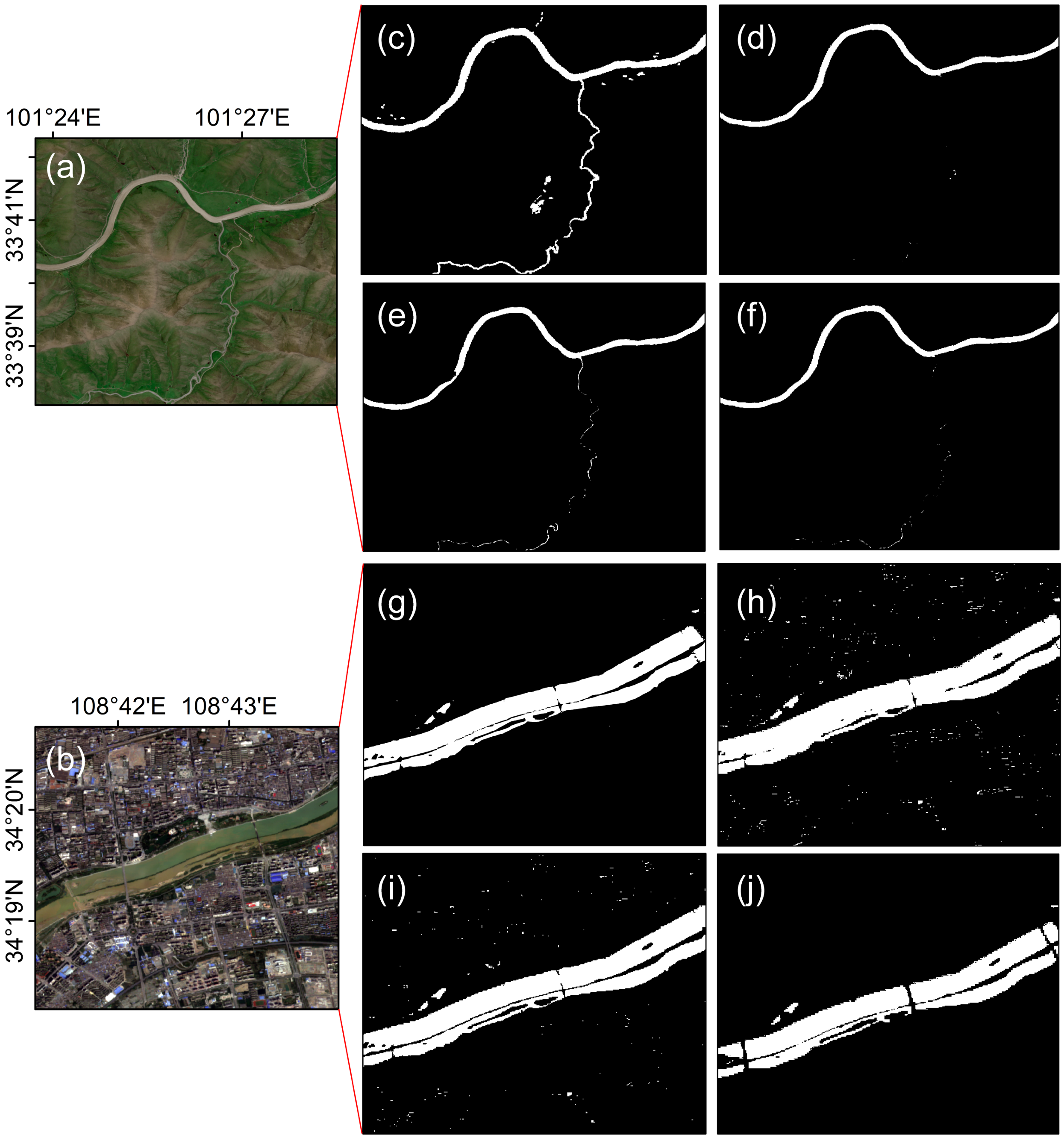

101°24'E
101°27'E
33°41'N
33°39'N
(a)
108°42'E
108°43'E
34°20'N
34°19'N
(b)
(c)
(d)
(e)
(f)
(g)
(h)
(i)
(j)

Figure 4.

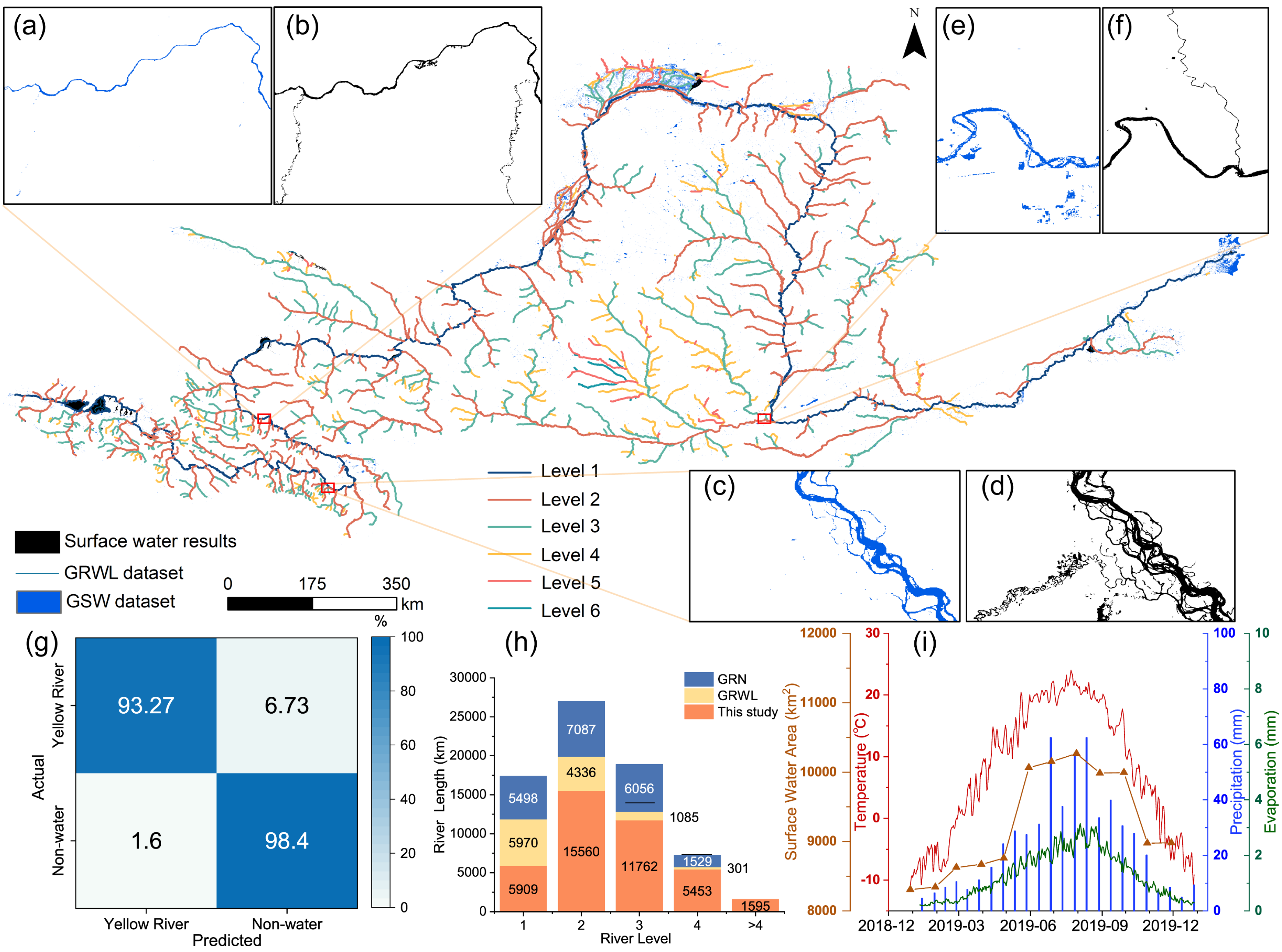

(a)
(b)
(c)
(d)
(e)
(f)
N
Level 1
Level 2
Level 3
Level 4
Level 5
Level 6
Surface water results
GRWL dataset
GSW dataset
0
175
350
km
(g)
Actual
Yellow River
Non-water
93.27
6.73
1.6
98.4
Predicted
%
(h)
GRN
GRWL
This study
River Length (km)
River Level
5498
5970
5909
7087
4336
15560
6056
1085
11762
1529
301
5453
1595
(i)
Surface Water Area (km²)
Temperature (°C)
Precipitation (mm)
Evaporation (mm)
2018-12
2019-03
2019-06
2019-09
2019-12